Journal of Architectural and Planning Research
37:3 (Summer, 2023) 31

BEYOND POINT CALIBRATION: IDENTIFIABILITY AND OBSERVABLE DESIGN IN DISCRETE ELEMENT CALIBRATION FOR NEAR-NOZZLE 3D CONCRETE PRINTING

Donald Shoup
Lijun Liu

Calibration studies for fresh cementitious materials are still commonly judged by whether one selected parameter set reproduces one or two macroscopic tests. Much less attention is paid to whether the chosen observables actually identify the underlying DEM micro-parameters in a unique and stable way. This issue is especially important for near-nozzle mixing in extrusion-based 3D concrete printing, where calibration must distinguish free-flowing aggregate behavior, fluid-like paste behavior, and cohesive mixed-mortar behavior within one workflow. Using the central composite design (CCD) data of as a secondary-analysis dataset, this study quantifies the identifiability gains obtained by enriched observables in DEM calibration. A total of 46 simulation runs were reanalyzed: 13 for Poraver®, 20 for paste, and 13 for mortar. Second-order response-surface surrogates were re-estimated, and admissible parameter regions were compared under competing observation schemes using feasible-set fraction, parameter-span reduction, and Pareto trade-off analysis. The reanalysis shows that observability is strongly material dependent within the CCD domain. For Poraver®, an angle-of-repose target alone leaves essentially the full restitution search width admissible at a 1% tolerance, whereas adding the pile-shape index reduces the feasible fraction of design space from 0.702% to 0.089% and contracts the admissible restitution width by 86.7%. For paste, slump diameter alone weakly constrains the friction parameters; both friction coefficients remain effectively unresolved over the search range, while low-cracking Pareto-efficient solutions concentrate in a narrow low-adhesion band and therefore motivate a better experimental crack descriptor. For mortar, the value of the standardized Haegermann sequence is pronounced: at a 2% tolerance, using only the fifteenth-stroke diameter leaves 11.755% of the parameter space admissible, whereas using the full d_5–d_{10}–d_{15} sequence reduces this fraction to 0.036% and confines the admissible surface-energy interval to $6.02\,\mathrm{J\,m^{-2}}$ *to* $6.40\,\mathrm{J\,m^{-2}}$*. The main contribution of enriched calibration protocols is therefore not only better fit, but materially improved parameter identifiability. Because the analysis is based on deterministic surrogates fitted within CCD bounds, the claims are comparative rather than universal; within that scope, the study offers a transparent framework for judging which experiments are genuinely informative in DEM calibration for additive manufacturing in construction.*

https://doi.org/10.66033/japr2022-303

INTRODUCTION

Extrusion-based additive manufacturing of cementitious materials is now established as a major branch of digital construction because it can reduce formwork dependency, enable geometric differentiation, and support more deliberate use of material across the built volume (Paolini et al., 2019; Pegna, 1997). Yet its computational analysis still depends critically on the fidelity of constitutive or particle-scale representations of fresh material behavior. Within DEM-based studies, important progress has been made in simulating fresh-concrete yield behavior, thixotropy, slump response, extrusion, and mixing (Krenzer et al., 2019; Li et al., 2018; Mechtcherine & Shyshko, 2015; Mu et al., 2023; Ramyar & Cusatis, 2022; Zhi et al., 2022). The calibration problem, however, remains fundamentally difficult because several combinations of micro-parameters may reproduce the same macroscopic test response (Fransen et al., 2022; Rackl & Hanley, 2017; Roessler et al., 2019).

This identifiability problem becomes more consequential in near-nozzle mixing systems for 3D concrete printing. Unlike conventional pre-mixed extrusion, near-nozzle mixing must represent at least three physically distinct states within one process chain: a free-flowing granular aggregate phase, a fluid-like paste phase, and a cohesive mixed mortar phase. addressed this challenge by calibrating Poraver®, paste, and mortar separately, using a two-step CCD-based protocol grounded in angle of repose (AoR), slump testing, and the Haegermann flow table test (H-FTT) (Daniel, 2019). Their contribution was methodologically significant in two ways. First, they introduced additional shape descriptors to refine AoR- and slump-based calibration. Second, they used the standardized H-FTT sequence to calibrate cohesive mortar through the diameters measured at the fifth, tenth, and fifteenth stroke (Daniel, 2019; German Institute for Standardisation, 2007).

What the original study did not quantify, however, is how much these additional observables improve parameter identifiability relative to simpler calibration choices. This omission is important. A calibration workflow can appear successful because it produces one parameter set with small output error, while still remaining underdetermined over a large region of the admissible parameter space. The literature on DEM calibration has repeatedly highlighted the existence of ambiguous parameter combinations and the value of design-of-experiments or surrogate-based methods for reducing computational cost (Chehreghani et al., 2017; Fransen et al., 2022; Rackl & Hanley, 2017; Roessler et al., 2019; Wilkinson et al., 2017). Yet, in construction-oriented DEM work, observable design itself has rarely been treated as the central research problem.

The present article develops that missing layer by performing a structured secondary analysis of the CCD results reported by (Daniel, 2019). The objective is not to recalibrate the source study, nor to propose an alternative numerical model, but to ask a sharper methodological question: *which observables actually identify the micro-parameters, and by how much within the design domain?* This question is addressed using the same material system, the same calibration targets, and the same CCD data already reported in the source study. By re-estimating response-surface surrogates and comparing admissible parameter regions under competing observational schemes, the paper separates two issues that are often conflated in DEM practice: obtaining one good fit and obtaining an inverse problem that is sufficiently constrained to support interpretation.

The contribution of the study is threefold. First, it provides a transparent identifiability analysis built directly on calibration data. Second, it shows that the practical value of enriched observables differs sharply across aggregate, paste, and mortar states, rather than improving all subproblems equally. Third, it derives concrete guidance on experimental design for future DEM calibration in additive manufacturing in construction. In methodological terms, the paper argues that the central calibration question is not only how to fit a DEM model efficiently, but how to select measurements that make the inverse problem materially better posed.

SOURCE DATASET AND ANALYTICAL FRAMEWORK

Calibration data used in the analysis

This study is a secondary analysis of the numerical data reported in the appendix tables of (Daniel, 2019). No new DEM simulations or laboratory experiments were conducted. The dataset consists of the full CCD design tables used in the source calibration: 13 runs for Poraver®, 20 runs for paste, and 13 runs for mortar, for a total of 46 runs. The corresponding experimental targets were also taken from the source paper: $\theta_{E,\mathrm{Po}} = 26.4^\circ$ for AoR, $D_{E,\mathrm{Pa}} = 385\,\mathrm{mm}$ for paste slump diameter, and $d_{E5} = 110.81\,\mathrm{mm}$, $d_{E10} = 122.45\,\mathrm{mm}$, and $d_{E15} = 131.95\,\mathrm{mm}$ for the H-FTT sequence (Daniel, 2019). For Poraver®, the experimental pile-shape index shown in the figure was used as $S_{E,\mathrm{Po}} = 154.75$ px, consistent with the source study's calibration logic (Daniel, 2019). All derived contractions reported below were recalculated from the admissible-set widths or feasible fractions and rounded consistently; because the analysis is limited to the CCD domain, the resulting conclusions concern within-domain identifiability rather than unrestricted global behavior.

The physical context of the source study is the gradation ready extrusion system (GRES), a near-nozzle mixing configuration in which lightweight expanded-glass aggregate and cement paste are combined at the nozzle before extrusion. The source paper modeled the granular Poraver® phase with the Hertz–Mindlin formulation and the paste/mortar phases with Hertz–Mindlin plus Johnson–Kendall–Roberts adhesion, reflecting the role of capillary or liquid-bridge forces in cohesive fresh material behavior (Alizadeh et al., 2018; Chen et al., 2019; Daniel, 2019; Johnson et al., 1971). Figure 1 reproduces the process context, while Figure 2 reproduces the calibrated H-FTT snapshots that motivate the sequential-observation analysis developed below. Table 1 summarizes the reanalyzed subproblems and the corresponding observables.

Table 1: Source calibration subproblems and observables used in the secondary analysis. All data were transcribed from .

Subproblem	Micro-parameters	run count	Experimental observables used in this study
Poraver®	e_{Po}, $\mu_{r,\mathrm{Po}}$	13	AoR $\theta_{E,\mathrm{Po}} = 26.4^\circ$; experimental shape index $S_{E,\mathrm{Po}} = 154.75$ px
Paste	$\mu_{s,\mathrm{Pa}}$, $\mu_{r,\mathrm{Pa}}$, γ_{Pa}	20	Slump diameter $D_{E,\mathrm{Pa}} = 385\,\mathrm{mm}$; predicted paste crack-shape index S_{Pa} used for Pareto analysis
Mortar	$\mu_{r,\mathrm{M}}$, γ_{M}	13	H-FTT diameters $d_{E5} = 110.81\,\mathrm{mm}$, $d_{E10} = 122.45\,\mathrm{mm}$, $d_{E15} = 131.95\,\mathrm{mm}$

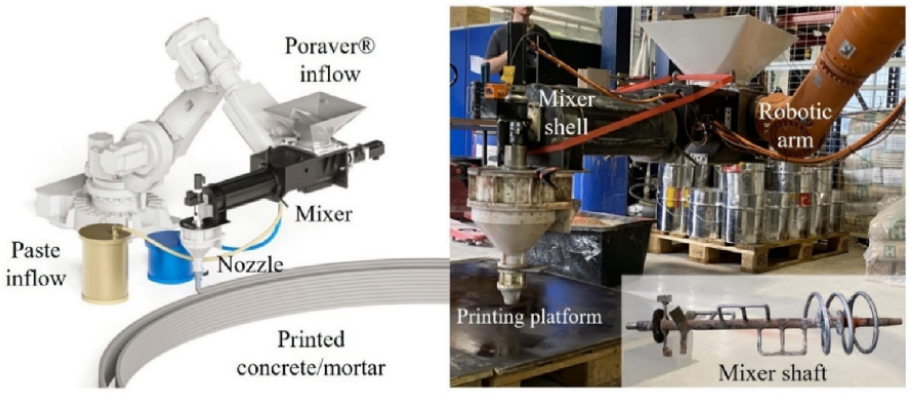

Figure 1: Near-nozzle mixing context used in the source study: rendering and prototype of the gradation ready extrusion system (GRES), including aggregate inflow, paste inflow, mixer shell, and extrusion region.

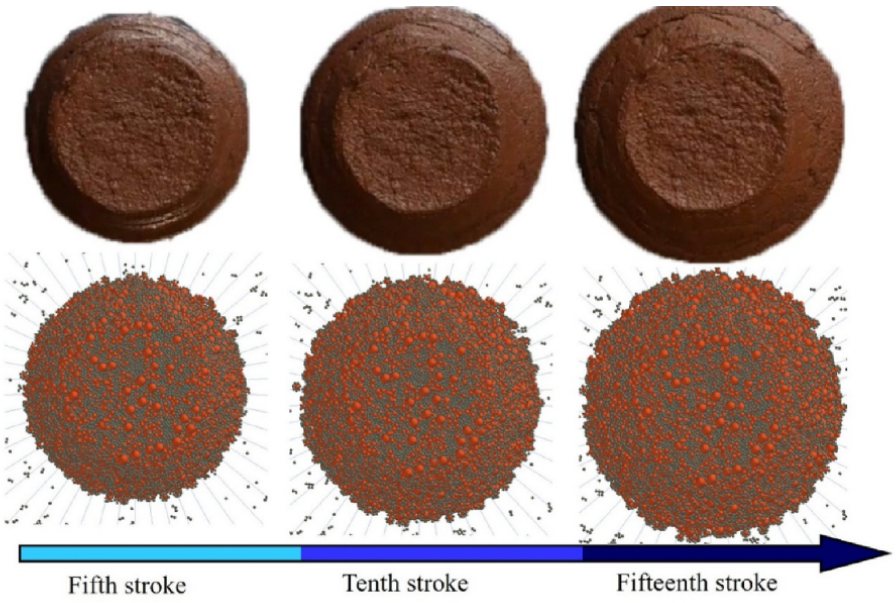

Figure 2: Mortar calibration states during the fifth, tenth, and fifteenth H-FTT stroke. These snapshots motivate the present study's emphasis on sequential observability rather than single-point matching.

Response-surface re-estimation

For each material state, second-order polynomial surrogates were re-estimated from the CCD tables. The general response-surface form was

$$\hat{y}(\mathbf{x}) = \beta_0 + \sum_{i=1}^{p} \beta_i x_i + \sum_{i=1}^{p} \beta_{ii} x_i^2 + \sum_{i<j} \beta_{ij} x_i x_j, \tag{1}$$

where $\mathbf{x}$ denotes the vector of DEM micro-parameters and $\hat{y}$ is the surrogate prediction for a given macro-response. For Poraver® and mortar, $p = 2$; for paste, $p = 3$. Ordinary least squares was used for all surrogate fits.

The purpose of this re-estimation was not to replace the original regressions, but to construct a transparent inverse-analysis layer directly from the CCD data. Fit quality was evaluated by R^2 and root-mean-square error (RMSE) on the run set. Because no additional runs outside the CCD tables were available, the surrogates were used comparatively within the bounds rather than as stand-alone predictive models beyond that domain.

Identifiability metrics

To quantify calibration ambiguity, the study defines an admissible set of micro-parameters for a tolerance ε as

$$\mathscr{A}_\varepsilon = \left\{ \mathbf{x} \in \Omega : \max_{k \in \mathscr{O}} \left(\frac{|\hat{y}_k(\mathbf{x}) - y_k^*|}{y_k^*} \right) \leq \varepsilon \right\}, \tag{2}$$

where Ω is the CCD search domain, $\mathscr{O}$ is the chosen observable set, and y_k^* denotes the corresponding experimental target.

Three complementary identifiability metrics were used.

1. *Feasible fraction*:

$$\Phi_\varepsilon = \frac{|\mathscr{A}_\varepsilon|}{|\Omega|}, \tag{3}$$

   approximated by dense grid sampling over the CCD bounds.

2. *Parameter span* for each parameter x_j:

$$W_j = \max_{\mathbf{x}\in\mathscr{A}_\varepsilon} x_j - \min_{\mathbf{x}\in\mathscr{A}_\varepsilon} x_j, \tag{4}$$

   which measures how narrowly the calibration problem localizes each micro-parameter.

3. *Pareto-efficient trade-off analysis* for paste, because the source study did not provide an experimental crack-shape target. In this case, solutions were evaluated simultaneously by slump-diameter error and predicted shape index S_{Pa}, and the non-dominated set was extracted within the design domain.

Scenario design

The identifiability experiments were defined to isolate the informational value of additional observables.

Poraver®. Two inverse problems were compared: (i) AoR only, and (ii) AoR plus the pile-shape index introduced in the source study.

Paste. Because the source paper used slump diameter as the experimental target and shape index as a qualitative regularizer, the reanalysis considered (i) diameter-only admissibility and (ii) Pareto-efficient solutions that jointly minimize diameter error and predicted edge cracking.

Mortar. Two cases were compared: (i) using only the fifteenth-stroke H-FTT diameter d_{15}, and (ii) using the full standardized sequence d_5–d_{10}–d_{15}.

The tolerance levels were selected to reveal identifiability structure at practically meaningful precision. A 1% tolerance was used for Poraver®, where the source pile-shape descriptor is most informative near the optimal ridge; a 2% tolerance was used for mortar to expose the contraction achieved by the H-FTT sequence; and a 5% tolerance was used for paste diameter admissibility, consistent with the broader uncertainty in the surrogate for the crack-shape response. The paired comparisons therefore use a fixed tolerance within each material state; the substantive claim concerns the relative contraction obtained by adding observables, not a direct ranking of absolute feasible fractions across different materials.

RESULTS

Surrogate fidelity

Table 2 reports the fidelity of the re-estimated response surfaces. The fits are excellent for AoR and mortar-diameter responses ($R^2 \geq 0.97$ except for d_5, which still exceeds 0.97 after rounding), strong for paste diameter, and appreciably weaker for paste shape index. This distinction matters methodologically. The first four responses support sharp admissibility analysis inside the CCD bounds, whereas the paste-shape index is better interpreted as a directional screening quantity. The revised analysis therefore uses the paste-shape surrogate to examine trade-off structure rather than to claim a sharply identified calibrated interval.

Table 2: Fit statistics of the re-estimated quadratic surrogates based on the CCD tables.

Response	R^2	RMSE
Poraver AoR, θ_{Po}	0.989	0.969
Poraver shape index, S_{Po}	0.974	3.980
Paste diameter, D_{Pa}	0.955	10.311
Paste shape index, S_{Pa}	0.632	7579.048
Mortar diameter, d_5	0.971	1.234
Mortar diameter, d_{10}	0.972	1.975
Mortar diameter, d_{15}	0.986	1.895

Poraver®: the pile-shape index suppresses a restitution ridge

The Poraver® subproblem reveals a classic equifinality pattern. At a 1% AoR tolerance, the admissible set occupies only 0.702% of the search domain, but that small fraction is misleading because it spans essentially the full restitution search width ($W(e_{\mathrm{Po}}) = 0.8485$) while restricting only rolling friction to a thin band. In other words, matching AoR alone does not identify e_{Po} in any practically useful sense; it merely defines a curved compensation ridge between restitution and rolling friction.

Once the pile-shape index is added, the feasible fraction drops to 0.089%, an 87.3% contraction relative to AoR-only matching. More importantly, the admissible restitution width contracts from 0.8485 to 0.1127 (an 86.7% reduction), and the admissible rolling-friction width contracts by 57.1%. Figure 3 shows this effect visually: AoR-only matching leaves a long U-shaped feasible ridge, whereas the joint AoR-plus-shape criterion confines the solution to the high-restitution branch near the choice.

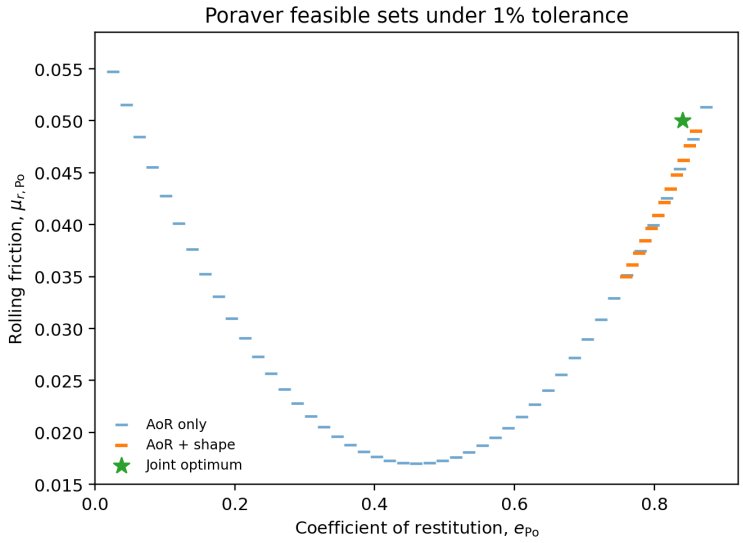

Figure 3: Poraver® feasible sets under a 1% tolerance. The light cloud denotes parameter pairs that reproduce the AoR target alone; the darker subset satisfies both AoR and the pile-shape target. The figure shows that shape information primarily resolves the restitution ambiguity left by AoR-only calibration.

This result clarifies the role of the shape index introduced. Its benefit is not merely aesthetic agreement between pile profiles. Rather, it acts as a genuinely informative observable that breaks an otherwise underdetermined

inverse problem. This conclusion is consistent with earlier calibration literature emphasizing ambiguous parameter combinations in DEM (Rackl & Hanley, 2017; Roessler et al., 2019), but here it is demonstrated directly within a construction-material setting.

Paste: slump diameter alone is weakly informative, and low-crack solutions form a narrow Pareto band

The paste subproblem is structurally different. The slump diameter surrogate is accurate enough for admissibility analysis ($R^2 = 0.955$), but the corresponding inverse problem is weakly informative. Under a 5% diameter tolerance, 8.38% of the full three-parameter search domain remains admissible. More revealingly, both friction coefficients remain effectively unresolved across their full search intervals, while the JKR surface energy is only weakly upper bounded ($\gamma_{\mathrm{Pa}} \lesssim 0.093\,\mathrm{J\,m^{-2}}$ in the reanalysis grid). Thus, slump diameter alone is insufficient to localize a unique paste parameter set.

Because the source paper used a crack-related shape index to regularize parameter selection, the present reanalysis examined the trade-off between slump-diameter error and predicted shape index. Figure 4 shows the resulting objective cloud and the Pareto front. A distinctive pattern emerges: low-crack Pareto-efficient solutions cluster in a narrow low-adhesion band. Restricting attention to Pareto-efficient solutions with less than 2% slump-diameter error yields the intervals

$$\mu_{s,\mathrm{Pa}} \in [0.052, 0.063], \quad \mu_{r,\mathrm{Pa}} \in [0.043, 0.060], \quad \gamma_{\mathrm{Pa}} \in [0.006, 0.015]\ \mathrm{J\,m^{-2}}.$$

These values should be interpreted as directional rather than definitive because the crack-shape surrogate has the lowest fidelity of all metamodels ($R^2 = 0.632$). Even so, the analysis reveals an important methodological point: the decisive missing ingredient for paste is not a more elaborate optimizer, but a more explicit experimental observable for edge integrity or crack morphology. The paste results are therefore most useful as evidence of observable insufficiency, not as a claim that the reported low-adhesion band is uniquely validated.

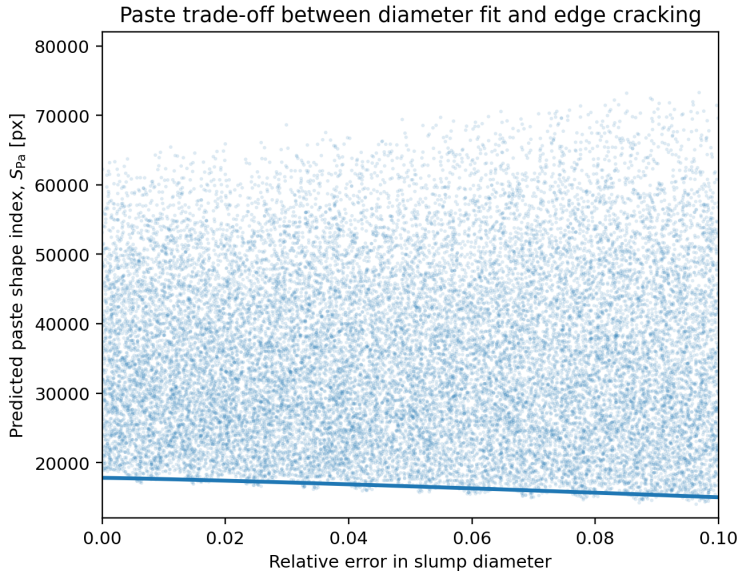

Figure 4: Trade-off structure for paste calibration. Each point is a grid-sampled parameter combination evaluated through the re-estimated surrogates. The lower boundary is the Pareto front between slump-diameter accuracy and predicted edge cracking. Although diameter alone is weakly informative, low-crack efficient solutions consistently favor low adhesion.

This outcome helps explain why paste calibration is intrinsically more fragile than the Poraver® and mortar subproblems. AoR and H-FTT both contain shape or temporal information that encodes process mechanics beyond a single scalar size measure. The slump diameter, by contrast, compresses rich flow morphology into one observable. Without an experimentally anchored crack descriptor, the inverse problem remains only partially identified.

Mortar: the multistage H-FTT sequence sharply reduces equifinality

The mortar results provide the clearest evidence for the value of enriched observables. If the calibration is performed using only the final H-FTT diameter d_{15}, then 11.755% of the search domain remains admissible under a 2% tolerance. This single-observable inverse problem leaves the full rolling-friction interval admissible and permits a very broad surface-energy band of width $11.69\,\mathrm{J\,m^{-2}}$. In practical terms, many materially different contact models can reproduce the final spread diameter.

When the full standardized sequence d_5–d_{10}–d_{15} is enforced, the admissible fraction collapses to 0.036%, which corresponds to a 99.7% contraction relative to d_{15}-only calibration. The admissible interval for $\mu_{r,\mathrm{M}}$ shrinks by 89.3%, and the admissible interval for γ_{M} shrinks by 96.8%. The remaining admissible band is tightly concentrated around

$$\mu_{r,\mathrm{M}} \in [0.076, 0.166], \qquad \gamma_{\mathrm{M}} \in [6.02, 6.40]\ \mathrm{J\,m^{-2}}.$$

As shown in Figure 5, the selection of ($\mu_{r,\mathrm{M}} = 0.2$, $\gamma_{\mathrm{M}} = 6.4\,\mathrm{J\,m^{-2}}$) lies just outside but immediately adjacent to this narrow multi-stroke band and is therefore more consistent with a shallow optimum basin than with a sharply isolated point (Daniel, 2019).

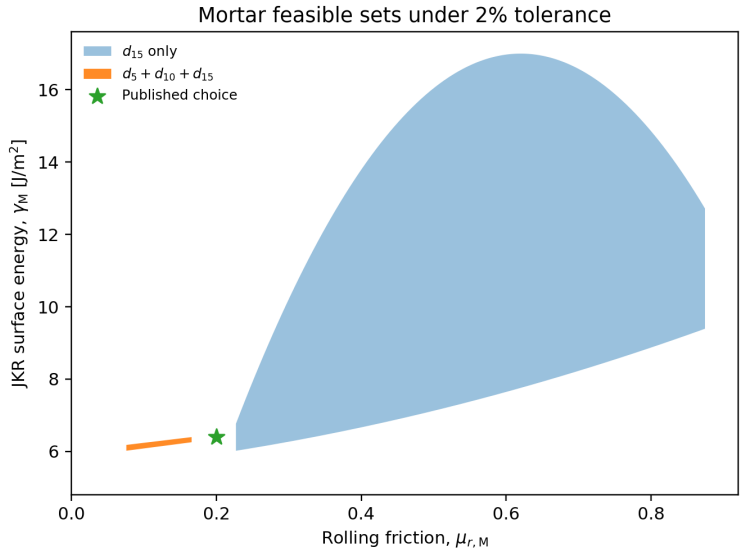

Figure 5: Mortar feasible sets under a 2% tolerance. The diffuse light region reproduces the fifteenth-stroke diameter only; the compact darker band satisfies the full d_5–d_{10}–d_{15} sequence. Sequential standard-based observables provide a major gain in parameter identifiability.

This result is especially important because it connects standardized testing to inverse-problem quality. The source paper introduced the H-FTT sequence because it better reflects mortar consistency under externally imposed perturbation (Daniel, 2019; German Institute for Standardisation, 2007). The present analysis shows

that the sequential measurement is also superior in a practical identifiability sense: it disambiguates parameter combinations that a final-diameter target alone cannot separate. In calibration terms, the standardized sequence behaves like a compact dynamic fingerprint of cohesive mortar behavior.

Summary of identifiability gains

Table 3 summarizes the principal identifiability reductions obtained by enriched observables in the Poraver® and mortar subproblems.

Table 3: Reduction in admissible parameter-space size when richer observables are enforced. Feasible fractions are computed on dense grids over the CCD parameter bounds.

Scenario	Feasible fraction [%]	Width of first parameter	Width of second parameter	Main contraction
Poraver AoR only (1%)	0.702	$W(e_{\mathrm{Po}}) = 0.8485$	$W(\mu_{r,\mathrm{Po}}) = 0.0397$	—
Poraver AoR + shape (1%)	0.089	$W(e_{\mathrm{Po}}) = 0.1127$	$W(\mu_{r,\mathrm{Po}}) = 0.0170$	Φ: -87.3%
Mortar d_{15} only (2%)	11.755	$W(\mu_{r,\mathrm{M}}) = 0.8485$	$W(\gamma_{\mathrm{M}}) = 11.6867$	—
Mortar $d_5 + d_{10} + d_{15}$ (2%)	0.036	$W(\mu_{r,\mathrm{M}}) = 0.0907$	$W(\gamma_{\mathrm{M}}) = 0.3778$	Φ: -99.7%

DISCUSSION

Observable design is a first-order calibration decision

The core message of the reanalysis is that DEM calibration quality depends as much on *what is measured* as on how the inverse problem is solved. In the literature, computational efficiency has often been the dominant motivation for CCD-, Kriging-, or metamodel-based calibration (Chehreghani et al., 2017; Fransen et al., 2022; Rackl & Hanley, 2017; Wilkinson et al., 2017). The present results suggest that this view is incomplete. A fast inverse procedure applied to weakly informative observables remains underdetermined. Conversely, a carefully chosen observable set can sharply contract the admissible region even with a simple quadratic surrogate.

In the near-nozzle mixing context, the implications are concrete. For aggregate calibration, scalar AoR is not enough; geometric profile information materially improves identifiability. For paste, single-diameter slump measurement is insufficient to localize friction and adhesion simultaneously; an experimentally anchored crack or edge-roughness observable would likely add disproportionate value. For mortar, the standardized H-FTT sequence is not merely convenient or conventional: it carries substantially more inverse information than a terminal spread measurement alone.

Why the gains differ across material states

The contrast among Poraver®, paste, and mortar is mechanistically meaningful. The AoR response of a free-flowing granular aggregate is governed largely by how restitution and rolling friction compensate in pile formation, which naturally produces a parameter ridge unless shape information is added (Al-Hashemi & Al-Amoudi, 2018; Tan et al., 2020). The paste slump, by contrast, collapses complex morphology into a single diameter and therefore suppresses much of the information needed to discriminate among frictional and adhesive contributions. Mortar lies in between, but the H-FTT sequence adds temporal structure: the fifth, tenth, and fifteenth strokes interrogate progressive rearrangement, densification, and loosening in a way that a

single final diameter cannot. This dynamic sensitivity likely explains the remarkable contraction observed for γ_M.

Methodological implications for future DEM studies of construction materials

Three practical recommendations follow. First, future DEM calibration studies should report not only one selected parameter set, but also admissible-set extent or equivalent uncertainty diagnostics. Second, the design of observables should be explicit. Measurements that capture profile, texture, or temporal evolution are likely to outperform purely scalar final-state metrics. Third, when rich observables are unavailable, secondary regularizers should ideally be tied to experimentally measurable descriptors rather than simulation-only heuristics. This point is most evident in the paste case.

The implications extend beyond the specific GRES system. Any DEM study of fresh concrete, mortar, or aggregate mixtures in additive manufacturing, pumping, or mixing can benefit from distinguishing between calibration *fit* and calibration *identifiability*. The former asks whether one parameter set works; the latter asks whether materially different parameter sets can be ruled out.

LIMITATIONS

This study has three limitations. First, it is a secondary analysis of CCD tables rather than a rerun of the full EDEM workflow. The analysis therefore inherits the design bounds, experimental conditions, and particle upscaling choices of the source paper (Daniel, 2019). Second, the paste crack-shape surrogate has only moderate fidelity, so the corresponding Pareto band should be interpreted as directional evidence of observable insufficiency rather than as a final calibrated interval. Third, the study analyzes deterministic surrogate predictions and does not propagate measurement noise or stochastic particle-generation variability. The results therefore quantify feasible-set contraction under the adopted tolerances rather than formal entropy reduction or full posterior uncertainty. These limitations do not alter the comparative conclusion, but they indicate the next logical step: coupling observable-design analysis with stochastic or Bayesian calibration (Fransen et al., 2022).

CONCLUSIONS

This article reanalyzed the CCD calibration data of to quantify how observable design influences parameter identifiability in DEM calibration for near-nozzle 3D concrete printing. Four main conclusions follow.

First, point calibration accuracy and parameter identifiability are not equivalent. A calibration may match experimental targets while still leaving a broad region of the parameter space admissible.

Second, the pile-shape index used for Poraver® is genuinely informative. At a 1% tolerance, it reduced the feasible fraction of the search space by 87.3% and reduced the admissible restitution width by 86.7% relative to AoR-only matching.

Third, paste slump diameter alone is weakly identifying. In the design domain, it leaves both friction parameters effectively unresolved and only weakly bounds the adhesion parameter. The low-crack efficient band is useful mainly as directional evidence that a measured secondary paste observable is needed.

Fourth, the standardized H-FTT sequence provides a major gain in mortar identifiability. At a 2% tolerance,

the full d_5–d_{10}–d_{15} sequence reduced the admissible fraction of the mortar parameter space from 11.755% to 0.036% and narrowed the admissible surface-energy interval to $6.02\,\mathrm{J\,m^{-2}}$ to $6.40\,\mathrm{J\,m^{-2}}$.

Taken together, these results show that richer observables are not merely refinements to an already adequate calibration procedure. Within the CCD domain, they are the main reason the inverse problem becomes sufficiently constrained to support reproducible and scientifically interpretable calibration decisions in additive manufacturing in construction.

DECLARATION OF COMPETING INTEREST

The authors declare no known competing financial interests or personal relationships that could have appeared to influence the work reported in this paper.

REFERENCES

Al-Hashemi, H. M. B., & Al-Amoudi, O. S. B. (2018). A review on the angle of repose of granular materials. *Powder Technology*, *330*, 397–417. https://doi.org/10.1016/j.powtec.2018.02.003

Alizadeh, M., Asachi, M., Ghadiri, M., Bayly, A., & Hassanpour, A. (2018). A methodology for calibration of DEM input parameters in simulation of segregation of powder mixtures, a special focus on adhesion. *Powder Technology*, *339*, 789–800. https://doi.org/10.1016/j.powtec.2018.08.028

Chehreghani, S., Noaparast, M., Rezai, B., & Shafaei, S. Z. (2017). Bonded-particle model calibration using response surface methodology. *Particuology*, *32*, 141–152. https://doi.org/10.1016/j.partic.2016.07.012

Chen, S., Liu, W., & Li, S. (2019). A fast adhesive discrete element method for random packings of fine particles. *Chemical Engineering Science*, *193*, 336–345. https://doi.org/10.1016/j.ces.2018.09.026

Daniel, K. A. (2019). Space-time description of supersonic jets with thermal non-uniformity.

Fransen, M. P., Langelaar, M., & Schott, D. L. (2022). Including stochastics in metamodel-based DEM model calibration. *Powder Technology*, *406*, 117400. https://doi.org/10.1016/j.powtec.2022.117400

German Institute for Standardisation. (2007). DIN EN 1015-3:2007-05, methods of test for mortar for masonry – part 3: Determination of consistence of fresh mortar (by flow table) [Beuth Verlag, Berlin].

Johnson, K. L., Kendall, K., & Roberts, A. D. (1971). Surface energy and the contact of elastic solids. *Proceedings of the Royal Society A: Mathematical, Physical and Engineering Sciences*, *324*(1558), 301–313. https://doi.org/10.1098/rspa.1971.0141

Krenzer, K., Mechtcherine, V., & Palzer, U. (2019). Simulating mixing processes of fresh concrete using the discrete element method (DEM) under consideration of water addition and changes in moisture distribution. *Cement and Concrete Research*, *115*, 274–282. https://doi.org/10.1016/j.cemconres.2018.05.012

Li, Z., Cao, G., & Guo, K. (2018). Numerical method for thixotropic behavior of fresh concrete. *Construction and Building Materials*, *187*, 931–941. https://doi.org/10.1016/j.conbuildmat.2018.07.201

Mechtcherine, V., & Shyshko, S. (2015). Simulating the behaviour of fresh concrete with the distinct element method–deriving model parameters related to the yield stress. *Cement and Concrete Composites*, *55*, 81–90. https://doi.org/10.1016/j.cemconcomp.2014.08.004

Mu, J., Li, Y., Hao, J., Liu, Y., & Shen, J. (2023). Research on discrete element simulation of slump test for fresh self-compacting concrete. *Journal of Building Engineering*, *70*, 106464. https://doi.org/10.1016/j.jobe.2023.106464

Paolini, A., Kollmannsberger, S., & Rank, E. (2019). Additive manufacturing in construction: A review on processes, applications, and digital planning methods. *Additive Manufacturing*, *30*, 100894. https://doi.org/10.1016/j.addma.2019.100894

Pegna, J. (1997). Exploratory investigation of solid freeform construction. *Automation in Construction*, *5*(5), 427–437. https://doi.org/10.1016/S0926-5805(96)00166-5

Rackl, M., & Hanley, K. J. (2017). A methodical calibration procedure for discrete element models. *Powder Technology*, *307*, 73–83. https://doi.org/10.1016/j.powtec.2016.11.048

Ramyar, E., & Cusatis, G. (2022). Discrete fresh concrete model for simulation of ordinary, self-consolidating, and printable concrete flow. *Journal of Engineering Mechanics*, *148*(3), 04021142. https://doi.org/10.1061/(ASCE)EM.1943-7889.0002059

Roessler, T., Richter, C., Katterfeld, A., & Will, F. (2019). Development of a standard calibration procedure for the DEM parameters of cohesionless bulk materials – part I: Solving the problem of ambiguous parameter combinations. *Powder Technology*, *343*, 803–812. https://doi.org/10.1016/j.powtec.2018.11.034

Tan, Y., Fottner, J., & Kessler, S. (2020). An efficient and reliable method for determining the angle of repose of biomass by using 3d scan. *Biomass and Bioenergy*, *132*, 105434. https://doi.org/10.1016/j.biombioe.2019.105434

Wilkinson, S. K., Turnbull, S. A., Yan, Z., Stitt, E. H., & Marigo, M. (2017). A parametric evaluation of powder flowability using a Freeman rheometer through statistical and sensitivity analysis: A discrete element method (DEM) study. *Computers & Chemical Engineering*, *97*, 161–174. https://doi.org/10.1016/j.compchemeng.2016.11.034

Zhi, P., Wu, Y.-C., Yang, Q., Kong, X., & Xiao, J. (2022). Effect of spiral blade geometry on 3d-printed concrete rheological properties and extrudability using discrete element modeling. *Automation in Construction*, *137*, 104199. https://doi.org/10.1016/j.autcon.2022.104199

AUTOBIOGRAPHICAL SKETCHES

Donald Shoup, Department of Urban Planning, University of California, Los Angeles, CA 90095-1656, USA

Lijun Liu, Department of Urban Planning, University of California, Los Angeles, CA 90095-1656, USA

Manuscript revisions completed 29 April 2023.